Structure and water oxidation activity of 3*d* metal oxides

Ye-Fei Li* and Zhi-Pan Liu*

Water splitting driven by solar energy is regarded as the candidate for the next generation of power source. The reaction is however kinetically hindered by the oxygen evolution reaction (OER) involving four proton–electron transfer steps. The ideal OER catalyst should avoid using precious elements, such as Ir, Ru, and Pt, and have a long-term stability under positive bias potential. Recent experiments have shown that most 3*d* oxides are OER active catalysts, while some can even achieve comparable activities to commercial Ir/Ru catalysts in lab condition. In this article, we review the recent theoretical progress for characterizing the structure of 3*d* oxides and understanding the photo-electrocatalytic water splitting mechanism over these catalysts. The methodology for global structure exploration, including evolutionary algorithm and stochastic surface walking method, is first introduced together with their applications in exploring the potential energy surface of TiO_2 and NiO_x systems. The current theoretical approaches to investigate the thermodynamics and kinetics of photo-/electrochemical reactions are discussed and the latest understanding for OER reactions are summarized. © 2015 John Wiley & Sons, Ltd

INTRODUCTION

Catalytic water splitting ($2H_2O \rightarrow O_2 + 2H_2$) that occurs under photo- or electrochemical conditions is regarded as a key process in the future global energy cycle to transform solar energy to storable chemical energy.[1–4] In the past few decades, it has attracted a great scientific interests, and much efforts have been devoted to the development of better anode catalysts for the oxygen evolution reaction (OER; $2H_2O \rightarrow O_2 + 4H^+ + 4e^-$), which has a high overpotential and incurs the major energy loss of the overall reaction. Abundant 3*d* transition metal oxides (including hydroxides) were commonly tested as the candidates of OER catalysts since TiO_2 was

discovered as the photocatalysts for OER. Because a large structural variety is generally present for these 3*d* materials and the OER activity could vary significantly depending on the catalyst preparation conditions, there has been a long debate on the active phase/sites that are responsible for OER activity, including the crystalline phases, surfaces, heterostructures and nanoparticle morphology. To design active and stable 3*d* metal oxides catalyst for OER remains to be a top challenge in the field.

Among 3*d* oxides, TiO_2-based catalyst as a prototypical photocatalyst has long been utilized as a model system to understand the mechanism of OER.[5–10] For its ambient condition stability and well-characterized crystalline structures, the structure–activity relationship of TiO_2-based catalysts has been studied in detail in recent years, focusing on O_2 evolution on various facets of TiO_2 phases. It is now generally accepted that OER is initiated by the formation of surface-trapped holes in the photocatalytic condition. These holes (h^+) oxidize water to O_2 via four proton–electron transfer (PET) steps, where adsorbed OH radical and peroxo species

*Correspondence to: yefeil@fudan.edu.cn; zpliu@fudan.edu.cn

Collaborative Innovation Center of Chemistry for Energy Material, Key Laboratory of Computational Physical Science (Ministry of Education), Shanghai Key Laboratory of Molecular Catalysis and Innovative Materials, Department of Chemistry, Fudan University, Shanghai, China

Conflict of interest: The authors have declared no conflicts of interest for this article.

are relevant intermediates for the first and second steps.[11–16] With this mechanism, several schemes have been proposed to improve photoactivity, such as doping, controlling the phase structures, and Lewis acidity.

Late transition metal oxides (Mn, Fe, Co, and Ni-based) belong to another important group of OER catalysts hotly studied in experiment recently. They are utilized as electrocatalysts, often at the alkaline conditions and, when combining with photon-adsorbing materials (such as Si crystalline), can split water using photon radiation energy. Because of the facile chemical synthesis and the abundance of the material, they have shown a great potential for practical applications with robust activity.[17–23] However, the active phase/structure of these late transition metal oxides are far less clear than TiO_2. Even the crystal structure can dynamically vary under potential bias, which can switch in between spinel, heterogenite, ramsdellite, and so on in alkaline solution.[24–29]

Recent years have seen a great progress in the development of new theoretical methods and their applications to the OER catalyzed by $3d$ metal oxide catalysts. The purpose of theoretical simulation is to identify the key structure units in the photocatalyst such as heterophase junction and to understand how the hole and electron transfer and activate molecules on the surface. However, the simulation of photocatalytic process on $3d$ metal oxides is often frustrated by some long-standing problems in theory, ranging from electronic structure calculations to the potential energy surface (PES) exploration. The band gap prediction and the hole-electron migration in the strong correlated systems are typical challenges for electronic structure calculation, whereas the presence of multiple structure funnels separated by high barriers for $3d$ oxides is a common difficulty for global structure exploration.

To motivate further scientific research in this emerging field, here we will review the recent literature and provide our latest theoretical thinking for the structure–activity relationship of $3d$ metal oxides in OER. We will first introduce the latest methodology development for resolving the PES of $3d$ metal oxides and for calculating the OER activity from first principles. The new physical/chemical insights obtained from recent theoretical investigations will then be highlighted together with the discussions on the technical difficulties for the future catalyst design. This review will focus on the two major types of OER systems, namely TiO_2-based system and the late-transition metal oxide system as represented by Ni oxide catalysts.

THEORETICAL METHODOLOGY

Methods for Structural Search and Pathway Sampling

An important feature of $3d$ metal oxides is their large structure variety. For example, TiO_2 is known to have many crystal phases, such as rutile, anatase, brookite, and TiO_2-B, which are stable at the ambient conditions. The heterophase junctions between the phases also have important catalytic role in the photocatalytic OER. It is no wonder that the recently developed structure search methods have been utilized for $3d$ metal oxide systems. While there are many structure search methods including basin-hopping method,[30] evolutionary (or genetic) algorithm,[31,32] metadynamics,[33,34] and stochastic surface walking (SSW) method,[35–37] here we will mainly introduce the genetic algorithm (GA) and the SSW method. The former one has been utilized to search for the crystal structure of Ni oxides and the latter one is recently utilized to search for the crystal phase transition pathways and the heterophase junction structure.

The basic idea of the evolutionary approach is to start from a set of structures, called population, and evolve them using selection and specially designed variation operators—i.e., recipes for creating offspring from parent structures. Variation operators, such as heredity (creates a child structure from two or more parents) and mutation (creates a child from a single parent), must retain some essential memory of parent structures in the offspring, while introducing new structural features. The initial population is usually created randomly, unless some information about the ground state is known, such as candidate structures, lattice parameters, or space group, and so forth. All structures created by the algorithm is then to be optimized at a chosen level of theory—e.g., empirical potentials, density functional theory (DFT), hybrid functionals, or Quantum Monte Carlo.

Exponential increase of the combinatorial complexity of the problem will lead to the decline in the quality and diversity of random structures with the increasing number of degrees of freedom. To deal with it, Oganov et al. proposed a new initialization scheme, as implemented in USPEX code.[31,38] The idea is to reduce the number of degrees of freedom by randomly applying symmetry to randomly generated atomic coordinates. This scheme can provide unbiased, highly diverse structures cover the configuration space better. In this procedure, during relaxation the initial symmetry of the structures can increase or decrease (to allow symmetry breaking,

they apply slight perturbations to the atomic positions). Variation operators also break symmetry and enable totally new structures with very different symmetries to emerge. Just improving initialization does not fully solve the problems of 'curse of dimensionality.' One has to improve the variation operators—so that not only good structures are given preference for creating offspring, but also good fragments of structures are identified and nurtured.

The most time-consuming step in the traditional GA loop is the local optimization of new offsprings. To speed up this step, Ho and Wang's group recently develop an adaptive-GA scheme.[32] In this approach, the optimization is performed using auxiliary classical potentials, whose parameters are fitted by a force-matching method with a stochastic simulated annealing algorithm, which utilizes energies, forces, and stresses of candidate structures obtained in the GA-loop calculated from first-principles DFT calculations as training database. After each GA loop, the auxiliary potentials parameters are readjusted. The use of such auxiliary potentials for structural relaxations could reduce significantly the computational time, and thus should have advantage to treat large system, e.g., reconstruction on surfaces and interfaces.

SSW method[35-37] is another powerful tool developed recently in our group for structural searching and pathway sampling. It is targeted for automated PES exploration of many-atom system. The SSW method is originally developed for molecules and clusters, and is recently extended to crystal systems by coupling the degrees of freedom of lattice. The method has been successfully utilized for predicting the structure of C_{100}-fullerene,[36] B_{40}-clusters,[39] the pathway of TiO_2(B)-to-anatase,[40] anatase-to-rutile,[41] and ZrO_2 t-m transitions.[42] A key feature for SSW method is the small displacement of atoms when exploring the PES, which allows it to maintain the one-to-one correspondence between two connecting minimum structures. The detail of the algorithm can be found in our previous publications.[35-37,43] Here, we briefly outline the central idea of SSW method and an illustration of the SSW method in 1-D PES is shown in Figure 1(a).

The SSW algorithm has an automated climbing mechanism to manipulate a structure configuration from a minimum to a high-energy configuration along one random mode direction, inherits the idea of bias-potential driven constrained-Broyden-dimer (BP-CBD) method for TS location.[44] In one particular SSW step, labeled as i, a modified PES V_{m-to-n} (n is the index of the bias potential, $n = 1,2,\ldots,H$), as shown in Eq. (1), is utilized for moving from the
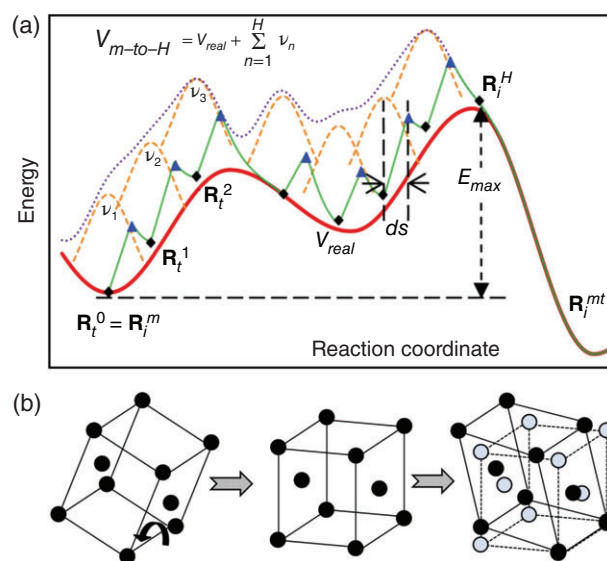

FIGURE 1 | The illustration of (a) the SSW method in 1D PES and (b) homogenous crystal phase transition. The phase transition can be divided into two steps: (1) the lattice rotation and (2) the lattice deformation. (Reprinted with permission from Ref 37. Copyright 2014 The Royal Society of Chemistry)

current minimum, $\mathbf{R}_i^m$ to a high energy configuration $\mathbf{R}_i^H$ (the climbing), in which a series of bias Gaussian potential v_n is added one by one consecutively along the direction $\mathbf{N}_i^n$.

$$V_{m-to-H} = V_{real} + \sum_{n=1}^{H} v_n = V_{real} + \sum_{n=1}^{H} w_n$$
$$\times \exp\left[- \left(\left(\mathbf{R}^t - \mathbf{R}_t^{\,n-1} \right) \cdot \mathbf{N}_t^{\,n} \right)^2 \Big/ {(2 \times ds^2)} \right] \quad (1)$$

where $\mathbf{R}$ is the coordination vector of the structure and V_{real} represents the unmodified PES; $\mathbf{R}_t^n$ are the nth local minima along the movement trajectory on the modified PES that is created after adding n Gaussian functions. The Gaussian function is controlled by its height w and its width ds, and is always added along one particular walking direction as defined by $\mathbf{N}^n$. Once the $\mathbf{R}_i^H$ is reached, all bias potential are removed and the local optimization is performed to quench the structure to a new minimum.

Because SSW method can maintain the pathway information when exploring PES, it is possible to utilize the SSW method to collect the neighboring minimum structure pairs, i.e., the initial state (IS) and the final state (FS) pairs. For crystal phase transition, the IS and FS correspond to two different crystal structures (phases), as illustrated in Figure 1(b). The

low-energy pathways linking the interested structures could then be resolved by using the double-ended transition state (TS) searching method to locate the TS. The recently-developed Double-Ended Surface Walking (DESW)[45] method aims for fast assessing the barrier height for a given IS/FS pair, which enables the method to fast analyze a large database of IS/FS pairs for the purpose of reaction pathway sampling. Similar to SSW method, the surface walking of DESW involves repeated bias potential addition and local relaxation with BP-CBD to correct the walking direction. Because there is no need to optimize the whole reaction pathway, the DESW method can be much less computationally demanding compared to the other double-ended methods and is applicable for reactions with complex PESs.

Methods for Calculating OER Thermodynamics and Kinetics

Water oxidation occurs on solid–water interfaces and thus the solvation effect must first be appropriately incorporated during simulations. The straightforward solution is to perform a long-time molecular dynamics (MD) simulation with a large quantity of explicit water molecules. It can capture both short-range (e.g., hydrogen bond) and long-range (e.g., dielectric screening) solvation effects. Obviously, the explicit water MD is highly computational demanding for sampling the solvent configurations, and more importantly, it is difficult to study the chemical reactions with high barriers where the chemical bond makes/breaks at the solid/liquid interface.[14]

To avoid the long-time MD simulation, several research groups have developed independently the periodic continuum solvation model based on the modified Poisson–Boltzmann equation,[46–50] namely CM-MPB as shown in Eqs (2) and (3). The dielectric constant ε depends on the electronic density distribution (Eq. (3)), which can be obtained from either the static atomic density of self-consistent density from DFT calculations. The continuum solvation can describe the long-range electrostatic interaction in solution and take into account the effect of electrolytes. It is also flexible to add a few explicit water molecules in the framework of continuum solvation to describe the short-range solvation interaction that is of quantum origin. The detailed implementation of CM-MPB method can be found in the previous publications.[16,51] It was also noticed that for oxide systems the dielectric constant ε could be lager than 1 within the slab due to the presence of tunnels or

holes in the bulk. Such unrealistic solvation effect needs to be removed by modifying the electronic density within the bulk,

$$\nabla \cdot (\varepsilon(r)\nabla(\psi)) = -4\pi\rho + 8\pi zec_b \frac{\sinh(ze\psi/kT)}{1 - v + v\cosh(ze\psi/kT)} \quad (2)$$

$$\varepsilon(\rho(r)) = 1 + \frac{\varepsilon_\infty - 1}{2}\left[1 + \frac{1 - (\rho(r)/\rho_0)^{2\beta}}{1 + (\rho(r)/\rho_0)^{2\beta}}\right] \quad (3)$$

To derive the free energy profile in photo-/electrochemical water oxidation, it is essential to include the temperature, pressure, and zero-point energy (ZPE) contributions. For adsorbants on solid surfaces, ZPE corrected ΔE is a good approximation to the Gibbs free energy (G), as the temperature (T) and pressure (p) contributions are small, while for oxygen, hydrogen, or water molecules, the large entropy term must be included in computing G. These corrections, i.e., $\Delta H_{0\to298K} - T\Delta S$ can be obtained from standard thermodynamic data and for H_2O and H_2, the value is –0.57 eV (H_2O) and –0.31 eV (H_2). The G of O_2 can then be derived as $G[O_2] = 4.92$ eV$+2G[H_2O] - 2G[H_2]$ according to the OER equilibrium at the standard conditions.

Then, we need to derive the Gibbs free energy change (ΔG) of an elementary step involving protons and holes shown in Eq. (4).

$$HA + hole^+ \to A + H^+(aq) \quad (4)$$

Equation (4) can be rewritten as

$$HA + hole^+ + e^- \to A + H^+(aq) + e^- \quad (5)$$
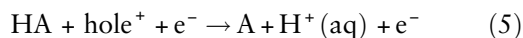
Using the chemical equilibrium relation in standard hydrogen electrode (SHE) $H^+ + e^- \to 1/2H_2$ (pH = 0, p = 1 bar, T = 298.15 K), one can establish that

$$\Delta G(H^+/H_2|SHE) = 1/2G[H_2] - G[H^+ + e^-] = 0 \quad (6)$$

Therefore, for the reaction in Eq. (5), the free energy change is written as follows:

$$\begin{aligned}\Delta G &= G[A] + G[H^+ + e^-] - G[HA] - G[h^+ + e^-] \\ &= G[A] + 1/2G[H_2] - G[HA] - |e|U \end{aligned} \quad (7)$$

where the U represents the electrochemical potential acting on the electron, from which the overpotential can be derived as U – 1.23 V.

The computation of the kinetics of the photo-/electro-catalytic reactions is much more challenging than that of thermodynamics, because it requires the correct description of the potential bias in electrocatalysis, and the energetics and localized behavior of electron/hole in photocatalysis. Several theoretical approaches have been developed in recent years to take into account explicitly the effect of potential bias in electrocatalysis,[49,50,52–63] such as the reaction center model,[64–69] double-reference method, and periodic continuum solvation model based on the modified Poisson-Boltzmann equation (CM-MPB).[46–50] The central idea of these methods is to adjust the potential bias by adding or removing a given number of electrons to or from the electrode. A key problem of this approach is how to deal with the compensate countercharge to maintain the charge neutrality of whole system as required in periodic systems. Three different approaches have been used in different methods, namely the countercharge ion (e.g., in reaction center model), the homogeneous countercharge background (e.g., in double reference model), and the Boltzmann distribution of the ionic charge outside the surface (e.g., with CM-MPB).

For the countercharge ion, as only integer charge can be applied it is difficult to control the potential precisely. In addition, this model is significantly different from the physical picture of the electrical double layer. For the homogeneous countercharge background, the fractional charge can be applied but it will inevitably introduce unphysical interaction since the countercharge exists everywhere in the system, including the bulk of electrode and thus deviate from the real picture of the electrical double layer. Fortunately, several benchmark studies have shown that this unphysical effect is limited for the screening effect in typical metal and metal oxide systems.[14]

In CM-MPB, the countercharge can be treated as the Boltzmann distributed ionic charge in electrical double layer, as described by the second term in the right-hand side of MPB. This approach avoids the unphysical effect caused by the countercharge, and also includes the electrostatic contribution of electric double layer. Liu group have implemented the CM-MPB in SIESTA code, where the countercharge in system is distributed following the MPB equation at the grid points of vacuum in the periodic slab calculation.[70] To accommodate the charges in MPB distribution, a large vacuum region along Z-axis is often required to separate the adjacent slabs. By this way, the electrochemical potential, i.e., of a system with a net charge q referring to SHE can be calculated using the computed work function in solution ($\Phi_{ref} - \Phi_F$),

the potential difference between the Fermi Level Φ_F and the potential level in solution Φ_{ref}.[70]

Different from electrocatalysis on metals, the photocatalysis on semiconducting materials does not involve fractional charge on surface, but localized photogenerated hole/electron with integer charge. The kinetics driven by these hole/electron is better described using the hopping picture involving charged particles. However, the commonly used local and semilocal DFT functionals, such as LDA and GGA, underestimates the band gap/levels and over-delocalizes the electron/hole states due to the well-known delocalization error.[71] They cannot be directly utilized for investigating photocatalysis. Instead, the post-LDA/GGA functionals, e.g., DFT + U or hybrid functional, must be utilized to localize the charge state and correct the band levels.

For cations with d and f electrons, the delocalization error can be largely corrected via the DFT + U scheme, where an effective parameter $U_{eff} = U - J$ is introduced to the electron–electron interaction potential of Hamiltonian as proposed by Dudarev et al.[72] The typical choices of U_{eff} for 3d oxides are listed in Table 1. As shown, all the U_{eff} values are in the range of 2–6 eV in PBE, but is system-dependent. The magnitude of U_{eff} can be determined from *ab initio* calculations, linear response theory or via the fitting to experimental thermodynamic data. In most cases, the U_{eff} obtained from different approaches are close, while in some case, such as Co_3O_4, the U_{eff} value derived from linear response theory is significantly larger than those fitted from

TABLE 1 | The U_{eff} (eV) and the Methods to Determine the Values in Literatures for Various 3d Oxides

Materials	U_{eff} (Methods)
TiO_2	3.5 (fit band gap),[73] 3.3 (linear response)[74]
V_2O_5	3.1 (fit formation enthalpy)[75]
Cr_2O_3	3.2[76] (*ab initio*)
FeO	3.5[76] (*ab initio*)
Fe_2O_3	4.3[76] (*ab initio*)
Fe_3O_4	3.3[77] (linear response)
Co_3O_4	2.0[78] (fit band gap), 3.3–3.5[79,80] (fit enthalpy), 5.9[81] (linear response)
NiOOH	5.5[77,82] (linear response)
CuO	9.79[83] (linear response)
ZnO	6–13 (fit PES expt.), 2–5.4[84] (fit GW or linear response)
MnO_x (x = 1–2)	4.0[85] (fit formation enthalpy, atomic magnetism, etc.)

experimental thermodynamic data. A recent study by Selcuk and Selloni shows that for Co_3O_4 (1 1 0), $U = 3.0$ eV provides a better overall description of the electronic structure and surface reactivity, whereas $U = 5.9$ eV is better suited for description of the magnetic properties.[86] Therefore, while U_{eff} value has explicit physical meaning and in principle the choice of U is not arbitrary, the experience is helpful to choose the best U_{eff} value for specific system and the benchmarking with experimental data is always essential in practice.

The delocalization error also exists on O $2p$ orbital, which is related to the hole at the valence band maximum (VBM), e.g., on TiO_2 and $BiVO_4$. It can also be localized using the DFT + U approach. It should be noticed that the physical meaning of such a correction remains under debate since the DFT + U is initially proposed for dealing with the strong correlation between d and f electrons. The hybrid DFT functionals, being orbital independent, could be the better choice for computing localized holes,[87] but their computational cost is generally too high, approximately 100-fold less efficient than DFT + U. This has severely limited its applications in heterogeneous photocatalysis. For these reasons DFT + U on O_{2p} has been practically utilized by several groups to investigate the migration of hole.[88–90] For instance, Deskin et al. have investigated the kinetics of hole transfer in rutile TiO_2.[88] The U_{eff} of 10 eV was utilized for O $2p$ orbitals of rutile, which is similar to the value for anatase TiO_2 determined from linear response theory.[89] It is obvious that the U value for $2p$ orbital is significantly larger than that for Ti $3d$.

APPLICATIONS

OER Mechanism on $3d$ Metal Oxides

As OER can occur under both photo and electrochemical conditions, the OER activity of solid catalysts has long been attributed to its oxidative level, i.e., the Fermi level for metal catalysts and the VBM for semiconducting catalysts, which must be larger than +1.23 V versus SHE (the reversible potential of OER). However, even for the most active commercial catalysts (e.g., RuO_2), an overpotential of ~0.3 V is required to overcome the barrier of OER and therefore the kinetics origin of the overpotential has been of intense scientific interests in the past decades. For example, TiO_2 as photocatalysts operating at the violet light adsorption region, its VBM is approximately +2.9 V versus SHE, far larger than 1.23 V and thus it can catalyze OER at the ambient condition with the photogenerated holes on the surfaces.

To investigate the thermodynamic PES, Nørskov and Rossmeisl proposed a four-step approach to analyze the key elementary step in OER.[91] It is assumed that OER follows four sequential PET steps, namely (1) $H_2O^* + h^+ \rightarrow {}^*OH + H^+$, (2) ${}^*OH + h^+ \rightarrow {}^*O + H^+$, (3) ${}^*O + H^+ \rightarrow {}^*OOH + H^+$, and (4) ${}^*OOH + H^+ \rightarrow O_2 + H^+$, representing the first, second, third, and fourth PET steps, respectively. The free energies for these elemental steps are ΔG_1, ΔG_2, ΔG_3, and ΔG_4. Under thermodynamics equilibrium conditions (1.23 V vs SHE), the best catalyst (zero overpotential) should not to require more than 1.23 eV for each electron transfer step. The overall overpotential can then be established as max $[\Delta G_1, \Delta G_2, \Delta G_3, \Delta G_4]/e – 1.23$ V. This approach, although neglecting the role of kinetic barrier in the reaction, can provide important information of the PES for OER on various photo-/electro-catalysts. In addition, this approach requires only static total energy calculations for H_2O^*, ${}^*OH$, ${}^*O$, *, ${}^*OOH$, H_2, and H_2O, and thus is suitable for large-scale catalyst screening of new OER catalysts. Along this line, Nørskov's group has proposed useful empirical rules to determine the OER activity based on the data fitting, e.g., the nearly linear relationship between the adsorption energy of O, OH, and OOH.[92,93] By investigating the thermodynamic PES on Rutile TiO_2 (1 1 0) using the above approach, they found that the OH production on TiO_2 surfaces is the rate determining step with an overpotential of 0.78 V.[15] The solution effect is often neglected when using the above thermodynamics analyses.

By incorporating the aqueous solution effect using CM-MPB method, Li et al. analyzed in detail the OER step-by-step on several anatase TiO_2 surfaces, including (1 0 1), (0 0 1), and (1 0 2).[16] The intermediate species, including adsorbed OH, O, bridging peroxo, and superoxo dimers were identified and their best adsorption structure were calculated. The reaction steps on anatase (1 0 1) surface are shown in Figure 2. The OER proceeds via the splitting of H_2O on the five-coordinated Ti (Ti_{5c}) site on surface to produce an adsorbed OH radical (state 2), and then loses another proton to form a bridge peroxo (state 3). The desorption of bridge peroxo to form O_2 is energetically highly unfavorable and therefore the second water molecule will adsorb at the surface Ti_{5c} nearby the bridging peroxo (state 4), which then decomposes to an adsorbed OH by losing a proton. At this step, the nearby bridging peroxo is converted to a terminal superoxo (state 5) as the adsorbed OH is negatively charged. Upon further losing a proton of the OH, the terminal O lean down to form a bridge O_3 (state 6). Finally, O_2 desorbs
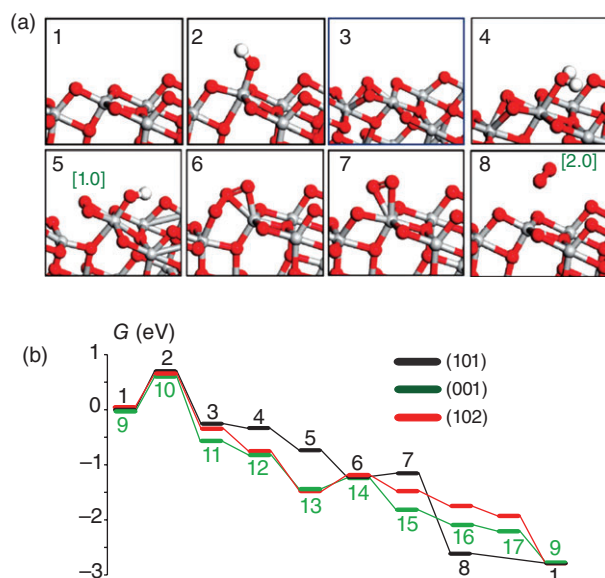
FIGURE 2 | (a) The optimized structures of the intermediate states of OER on anatase (1 0 1); (b) free energy profiles of OER on (1 0 1) (black), (0 0 1) (green), and (1 0 2) (red) surfaces at an overpotential of 0.7 V (1.93 V vs SHE) Ti, gray; O, red; H, white. (Reprinted with permission from Ref 16. Copyright 2010 American Chemical Society)

from the surface via a TS (state 7) with a very low reaction barrier (0.1 eV). It might be mentioned that the bridging peroxo state were later observed in experiment when anatase (1 0 1) with subsurface O vacancy is exposed to O_2, which suggests that peroxo might be a common species on anatase surfaces.[94] As for the OER on other anatase surfaces, the energetics appears remarkably similar (see Figure 2(b)), although the detailed intermediate states might vary. It suggests that the catalytic activity of different anatase surfaces is in fact not so different as long as the hole is present on the surface. It was concluded that the hole concentration on different surfaces should be the key factor for the photoactivity.

The OER PES in Figure 2(b) suggests that the generation of adsorbed OH radical from water is undoubtedly the most difficult step, which requires 1.39, 1.33, and 1.31 eV on anatase (1 0 1), (1 0 2), and (0 0 1), respectively, at the zero overpotential (1.23 V). This implies that at least 0.7 V overpotential is required on TiO_2 surfaces. The OER energetics on rutile (1 1 0) was also analyzed by Valdés et al., who found that the first PET ($H_2O* + h^+ \rightarrow *OH + H^+(aq)$) is the rate determining step with an overpotential of 0.78 V.[15] It was now generally accepted that the production of unstable OH radical is an important feature on TiO_2 photocatalyst and is the rate-determining step in the overall

OER kinetics. Along this line, Li and Liu also analyzed the OER on different anatase decahedron nanoparticles and found that the sharp anatase nanoparticles are significantly more active than the flat particles because of the enhanced OH adsorption ability. The most active anatase particle for OER is thus predicted to be 15−20 nm size.[95] More recently, Lee and Selloni investigated OER PES on anatase (0 0 1) on polar substrate $SrTiO_3$.[96] They show that the polarization of the substrate can significantly increase the OER activity by modifying the thermodynamics.

Using PBE0 hybrid functional and an explicit water solution model, Li and Selloni studied in detail the kinetics of the first PET step on anatase (1 0 1) in order to clarify the sequence of the proton and the electron transfer.[14] They constructed the PES corresponding to two electronic states relevant to the electron transfer, i.e., the state with the hole localized on an adsorbed water molecule (denoted water-hole state), and that with the hole localized on a adjacent surface threefold coordinated oxygen atom (denoted surface-hole state). The calculated energetic profiles are illustrated in Figure 3. The energetic profiles for the surface-hole and water-hole states become essentially degenerate around the FS of proton transfer, suggesting that the proton and electron transfer in the first PET is sequential, the electron transfer occurring preferentially after the proton transfer. The result also shows the subsequent electron transfer has a significantly lower barrier than that of the proton transfer. Thus, the proton transfer is the rate-determining step. Combining MD simulation based on DFT and free energy perturbation methods, Chen et al. have calculated the acidity constants for the acidity reaction: $Ti_{5c}OH_2 \rightarrow Ti_{5c}OH^- + H^+(aq)$ (pKa_1) and the basicity reaction: $OH_b^+ \rightarrow O_b + H^+(aq)$ (pKa_2) (OH_b represents the state with an extra H atom on TiO_2 bridging O).[97] The pKa_1 and pKa_2 are calculated to be 9 and −1, leading to the theoretical point of zero charge (PZC) of 4, being consistent with the experimental value (4.5−5.5). This indicates that under pH > 4 condition, the $Ti_{5c}OH^-$ species will accumulate on TiO_2 surface and this effectively promotes the first PET step of OER. These theoretical results explains nicely that the OER on TiO_2 is highly sensitive to pH of solution, which has been observed in experiment using both transient absorption spectroscopy[85,98,99] and photoluminescence measurements.[11]

Cheng et al. have investigated the trapping nature of photo-induced holes on rutile TiO_2 (1 1 0) water interface using hybrid DFT MD simulation.[87]
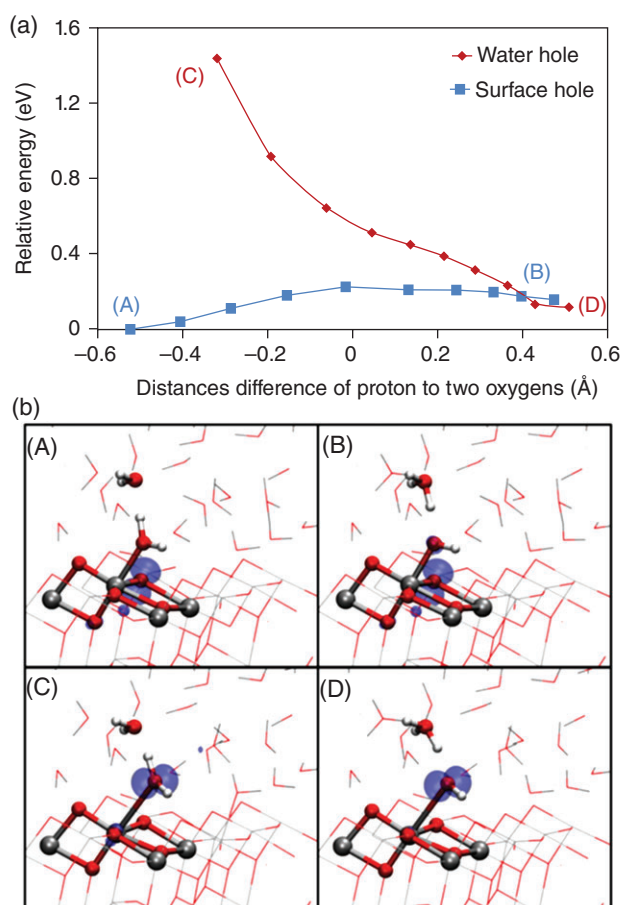
(a)

(b)

FIGURE 3 | (a) Proton-transfer energy profiles in the surface-hole (A, B) and water-hole (C, D) states for a selected configurations along the first principles MD trajectory of an anatase TiO$_2$ (1 0 1) slab in contact with liquid water. (b) Spin density (0.01 a.u. contour) of the water-hole and surface-hole states before and after the proton transfer. (Reprinted with permission from Ref 14. Copyright 2013 American Chemical Society)

They found the holes could be steadily trapped on terminal OH$^-$ on Ti$_{5c}$, and the resulting terminal TiOH$^{\bullet}$ is not stable and can spontaneously deprotonate to form more stable TiO$^{\bullet-}$ and OH$_b^+$ pair in water solution (pH = 7). In addition, they assigned the vertical and adiabatic energy levels associated with the two trapped hole states and the calculated LUMO – VBM gaps of the terminal TiO$^{\bullet-}$ and TiOH$^{\bullet}$ are consistent with the data measured from the TAS experiment that reveals two deeply trapped holes at 450 nm (2.8 eV) and 520 nm (2.4 eV).[98,100,101] These hole trapping states, TiO$^{\bullet-}$ and TiOH$^{\bullet}$, are thus expected to be pH-dependent.

To understand the structure sensitivity of OER, Zhao and Liu compared the first proton removal kinetics on two TiO$_2$ surfaces, rutile (1 1 0) and anatase (1 0 1) using the charged-slab CM-MPB method

with DFT PBE functional.[102] They found that the photo-induced hole cannot promote the O—H bond breaking of water. Instead, the O—H bond splitting of water is a surface catalytic reaction driven by heat on both TiO$_2$ surfaces. The hole-transfer occurs after the water dissociation when the surface O nearby the dissociated OH anion traps the hole, which is consistent with the conclusion by Li and Selloni.[14] The results show that the photocatalytic water splitting on TiO$_2$ is both surface- and phase-sensitive. The rutile (1 1 0) surface is more active for water splitting kinetically compared to anatase (1 0 1), with the calculated barrier of O—H bond breaking on rutile being approximately 0.2 eV lower than on anatase.

The thermodynamics analysis has recently been extended to understand the origin of the OER activity of other 3d oxides, such as MnO$_x$, Fe,O$_x$, CoO$_x$, and NiO$_x$. Li and Selloni carried out DFT + U calculations for OER on six selected surfaces, namely pure/Fe-doped β-NiOOH($01\bar{1}5$), pure/Fe-doped γ-NiOOH (1 0 1), NiFe$_2$O$_4$ (1 0 0), and Fe$_3$O$_4$ (1 0 0).[77] They found that Fe-doped β-NiOOH ($01\bar{1}5$) and NiFe$_2$O$_4$ (1 0 0) are two most active surfaces for the OER, with theoretical overpotentials of 0.26 and 0.42 V, respectively. The others have the overpotential of at least 0.47 V. The OER mechanism remains to be similar to those occurring on TiO$_2$ surfaces except that the adsorbed OH species becomes much more stable on these late transition metal oxide surfaces. The free energy change for the first PET step is at most 1.69 eV (on β-NiOOH($01\bar{1}5$)), much smaller than that on anatase (2.54 eV on (1 0 2)[16]) and rutile surfaces (2.01 eV on (1 1 0)[15]). This enhanced adsorption of OH on late transition metal oxides can be attributed to the partially occupied e$_g$ orbitals, which can develop strong covalent bonding with O 2p orbitals of OH. Liao et al. have investigated the OER mechanism on hematite (0 0 0 1) surface and found an overpotential of 0.77 V for the surface.[103] In addition, they consider cation doping by substitution of Fe by Ti, Mn, Co, Ni, and Si, and anion doping of F by replacing O. They show that Co- or Ni-doped hematite surfaces provide the most thermodynamically favored reaction pathways. Bajdich et al.[104] calculated the volume Pourbaix diagram of layered and spinel bulk phases of Co oxides as a function of applied potential and pH, and found that β-CoOOH is the active phase where the OER occurs in alkaline media, in agreement with the recently reported experimental data.[105] The thermodynamically stable surface of β-CoOOH exposed under OER condition depends on pH and applied potential. At the low potential, (1 0 1 4) surface covered by 1 monolayer

H$_2$O is the most stable surface, and (0 1 1 2) terminated by 1 monolayer of O is the most stable one at the high potential. The calculated overpotential for (1 0 1 4) and (0 1 1 2) are 0.48 and 0.80 V, respectively. The overpotential for the OER can be reduced to 0.36 V by doping the (1 0 1 4) surface with Ni, whereas doping the (0 1 1 2) surface with V can reduce the overpotential to 0.53V.

Unlike the other 3d oxides, MnO$_x$ has rich polymorph and oxidation state (from +2 to +4), and thus its structure–activity relations are more complex than other 3d oxides. Su et al.[106] constructed surface Pourbaix diagrams on Mn$_3$O$_4$ (0 0 1), Mn$_2$O$_3$ (1 1 0), MnO$_2$ (1 1 0) and MnO (1 0 0), and calculated the overpotentials of the surfaces. They revealed that the active surface for OER is O covered MnO$_2$. From these theoretical results, we can summarize that undoped late 3d oxides generally have an overpotential of at least approximately 0.5 V, significantly lower than that of TiO$_2$ (~1.4 V) but still too high for industrial application. Mixing or doping of 3d oxides with other elements at optimal ratio could be a practical solution toward the reduction of OER overpotential.

Structures of 3d Metal Oxides

Bulk Structure

First-principles-based crystal structure prediction is one of the most exciting advances in the last 10 years, which has led to many successes in predicting new high-pressure materials. Thanks to the methodology advance and high-performance computing facilities, the first principles method in combination of global optimization techniques can now be routinely utilized for the crystal structure prediction at an unit cell size below approximately 40 atoms. The methods for predicting the heterophase junction and the solid–solid phase transition pathways are also recently developed and applied to TiO$_2$ systems based on the extensive pathway sampling between the crystal phases.

Using SSW method in combination with Wang-Landau crystal phase density sampling, Shang et al. recently explores the PES of TiO$_2$ crystals aiming to find new TiO$_2$ phases with better photocatalytic activity at the visible light regime, i.e., with reduced band gap for better solar energy adsorption.[107] The common TiO$_2$ phases identified from SSW simulation are as shown in Figure 4(a). While there are indeed five new phases identified for TiO$_2$, they are in general not the most stable phase in the pressure phase diagram. Theoretical calculations show that high-pressure phases, #110, pyrite and fluorite, have narrower band gap than rutile, but they are very unstable at the low-pressure condition. This indicates that pure TiO$_2$ phases that are stable at ambient conditions are unlikely to exhibit the desired visible light adsorption behavior. The combination of differently structured oxide materials, such as the material with heterophase junction, is more practical for the design of new photocatalyst.

The lowest energy phase transition pathways connecting to the abundant phases, i.e., rutile and anatase, were then searched using SSW-based pathway sampling, as shown in Figure 4(b). The high-pressure phase, α-PbO$_2$-type TiO$_2$-II is found to act as the key intermediate in between rutile and anatase phase transition. The anatase-to-rutile transition
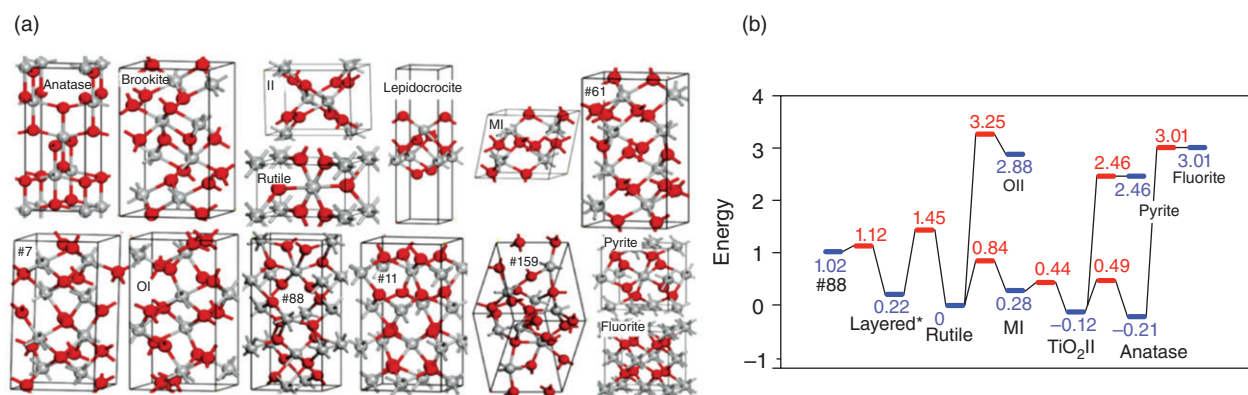

FIGURE 4 | (a) DFT-optimized bulk phase structure identified from SSW-crystal global optimization. Gray and red spheres represent Ti and O atoms, respectively. (b) The DFT lowest energy connectivity map of the major phases at zero pressure. The energy unit is eV per Ti$_4$O$_8$ cell. The energy of rutile is set to zero. *lepidocrocite typed layered structure (*Pmmn*, #59). (Reprinted with permission from Ref 107. Copyright 2015 Institute of Physics.

occurs following the crystallographic orientation relationship (OR), namely, rutile(1 0 1)//TiO$_2$-II (0 0 1), and TiO$_2$-II(1 0 0)//anatase(1 1 2). A mixed phase, anatase-TiO$_2$(II), is shown to have balanced properties for photoacticity, i.e., with good stability and narrower band gap compared to anatase phases.

Unlike TiO$_2$, the late transition metal oxides are often present as layered hydroxide phase, which yields a large surface area for the catalysts. A significant structure variety is also common to these oxide systems, particularly because the cations of late transition metals can be redox active. Because of the intrinsic difficulty of first principles DFT calculation for the strong correlated systems, there are few studies on the PES of 3d late transition metal oxides. Li and Selloni performed the crystal structure exploration for β-NiOOH system using generic algorithm as implemented in USPEX.[82] They utilized the dispersion-corrected hybrid functional calculations for describing the Ni oxides, which were found to be essential to predict the energy order of different phases. They identified two groups of favorable structures for β-NiOOH, as shown in Figure 5. The first group includes layered structures with alternate Ni(OH)$_2$ and NiO$_2$ layers, consistent with the experimental observation using high resolution Transmission Electron Microscopy (HRTEM), while the other one includes tunnel structures isostructural with MnO$_2$ polymorphs. For the tunnel structures, the structure 3 is isostructural with pyrolusite; the structure 4 is isostructural with nsutite; and the structure

9 is isostructural with ramsdellite. The coexistence of tunnel structures with the layered structures can rationalize the mosaic textures observed in HRTEM. The phase transitions between the two groups of structure are possible at the ambient conditions as observed in experiment, which is important to the stability of the oxides. Further studies are required to establish the low energy pathways connecting these phases.

From the bulk TiO$_2$ and β-NiOOH structures, one can immediately notice that most of the structures identified from PES exploration are in fact isostructural with known mineral structures of other metal elements, such as lepidocrocite, pyrite, fluorite, α-PbO$_2$, nsutite, pyrolusite, ramsdellite, and so on. It is thus confirmed that common rules are followed to build the crystal structures, where the ion size, oxidation state, and coordination configurations are key factors to determine the stability of crystal structure. These similarities also suggest that the known crystal structures are good initial guess in the global structure search, which could significantly speed up the finding of unknown crystal structures.

Heterophase Junction Structure

While mixed phase TiO$_2$ oxides such as the commercial P25 catalysts are practically utilized as photocatalysts for their higher activity than single-crystal oxide, it is not until recent years that the presence of phase junction is recognized as a main cause for the enhanced photoactivity in the mixed oxides. The phase junction can not only improve the ability of
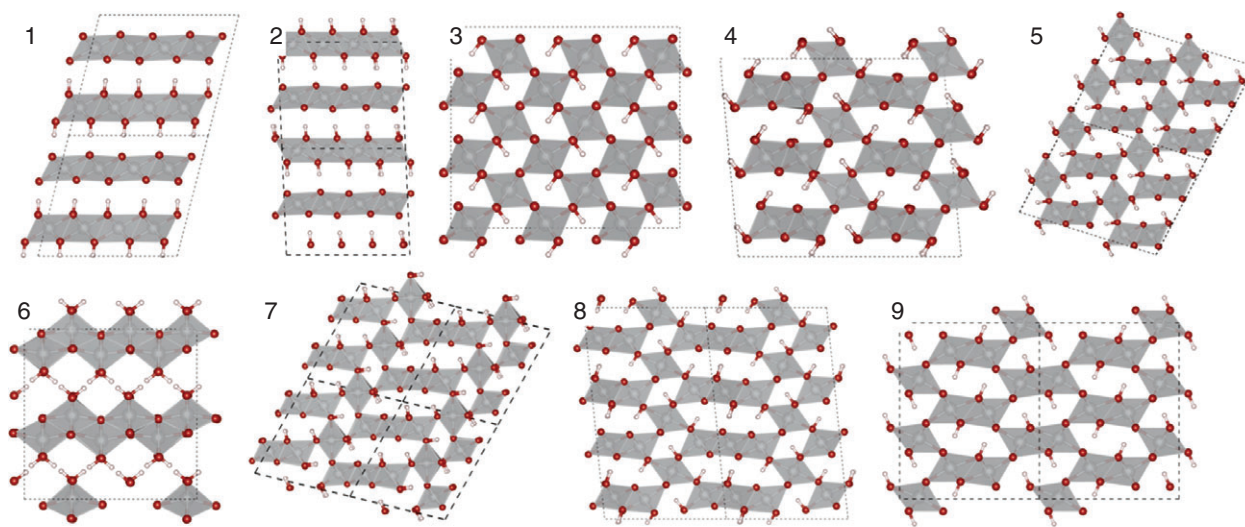

FIGURE 5 | Energetically favorable NiO$_6$ octahedral frameworks for β-NiOOH. 3: pyrolusite (rutile), 4: nsutite, 5: ramsdellite-/pyrolusite-type intergrowth, 6: lepidocrocite, 7–8: 1 × 3 tunnel/pyrolusite-type intergrowth, 9: ramsdellite. (Reprinted with permission from Ref 82. Copyright 2014 American Chemical Society)

solar energy harvesting but also facilitate the subsequent chemical reactions, e.g., those related to pollutant decomposition. Because the structurally disordered interface with the stacking faults or dislocations can trap photo-generated charges[108] and not beneficial in photocatalysis, it is a general concern on how to synthesize high quality, structurally ordered interface at the atomic level. Experimentally, the heterostructure materials can be prepared via different approaches, including the partial solid-to-solid phase transition, the colloidal seed-growth[109–112] and chemical vapor deposition second-growth.[113,114] Among them, the partial solid-to-solid phase is technically simple and widely used for synthesizing mixed phase photocatalysts, but it is also more difficult to control the structure of the junction. The determination of these structures at the atomic level has long been of great challenge for both experiment and theory.

Very recently, Liu group proposed a new method to determine the structure of heterophase junction, which is based on the extensive SSW crystal pathway sampling. The method has been first applied to TiO$_2$-B/anatase biphase system, where the theoretical prediction of the heterophase junction is compared with the HRTEM experiment observation. TiO$_2$-B is a metastable phase and can transit to anatase by heating. This enables the fabrication of TiO$_2$-B/anatase phase junction by partial phase transition at the high temperature. As the photocatalyst for water splitting and pollutant control, TiO$_2$-B based systems have been studied by many research groups.[115–122] It was reported that the presence of TiO$_2$-B/anatase phase junction in the nanofiber can dramatically increase the photoactivity of the catalyst.[118]

To clarify the structure of the heterophase phase junction, Zhu et al. utilized SSW pathway sampling to determine the lowest pathway from TiO$_2$-B to anatase.[40] As shown in Figure 6, the lowest energy pathway is a straightforward one-step reaction with a barrier of only 0.12 eV per TiO$_2$ unit. The other transition pathways leaving TiO$_2$-B phase are energetically much higher. It was found that the atomic habit planes (coherent interface) of the phase transition (blue dotted line, Figure 7) is TiO$_2$-B ($\bar{2}$ 0 1) and anatase (1 0 3). The OR of TiO$_2$-B/anatase transition is thus written as ($\bar{2}$ 0 1)$_B$//(1 0 3)$_A$, [0 1 0]$_B$//[0 1 0]$_A$. According to the OR, the phase junction can be constructed by attaching ($\bar{2}$ 0 1)$_B$ with (1 0 3)$_A$. The theoretical OR for the phase transition was proved by HRTEM observation of the TiO$_2$-B/anatase bicrystalline material. It was concluded that TiO$_2$-B/anatase phase junction can be regarded as a perfect phase

junction that lacks of the common stacking faults or dislocation defects, those otherwise are commonly present during the growth and packing of crystals.[123]

Different from the TiO$_2$-B to anatase transition, the pathway from anatase to rutile phase transition is much more complex, involving multiple intermediates as shown in Figure 4(b). The heterophase junctions in anatase/rutile biphase catalysts are thus more complex. From the crystal phase transition pathways, Zhao et al. present a three-phase atomic model for the anatase−rutile TiO$_2$ heterophase junction using TiO$_2$-II phase as the intermediate,[89] which is suggested to be a layer-by-layer 'T-shaped' anatase/TiO$_2$-II/rutile junction. The intermediate TiO$_2$-II phase, although predicted to be only a few atomic layers thick in contact with anatase, is critical to alleviate the interfacial strain and to modulate photoactivity. Importantly, these three-phase junctions can act as a single-way valve in photocatalysis, allowing the photo-generated hole transfer from anatase to rutile but frustrating the photoelectron flow in the opposite direction, which otherwise cannot be achieved by the anatase−rutile direct junction. This new model clarifies the roles of anatase, rutile, and the phase junction in achieving high photoactivity synergistically and provides the theoretical basis for the design of better photocatalysts by exploiting multi-phase junctions.

These anatase/rutile heterophase junctions synthesized from the heat-driven partial phase transition should be geometrically close to the anatase surfaces in order to modulate efficiently the electron/hole separation. To identify the nucleation site of rutile formation where the heterophase junction grows initially, recently Liu group further characterized the atomic structure of the nucleation sites in the TiO$_2$ anatase-to-rutile phase transition by extending SSW based pathway sampling for exploring surface reconstruction channels.[41] The lowest energy pathways at the initial stage of phase transition, as shown in Figure 7, occurs on (1 1 2) ridged surface, which can lead to the formation of both TiO$_2$(II) and brookite thin slabs. The other anatase surfaces, although may reconstruct, do not lead to the formation of new phases (the best known example is anatase (0 0 1) surface, where recent experiment studies provide new model for the (1 × 4) reconstruction on the top surface layer,[124,125] originally rationalized by the added molecule (ADM) model[126]). The TiO$_2$(II) phase is kinetically preferred product, the propagation of which into subsurface is still hindered by high barriers that is the origin for the slow kinetics of nuclei formation. The rutile nuclei are thus not rutile phase but nascent metastable TiO2-II phase in anatase
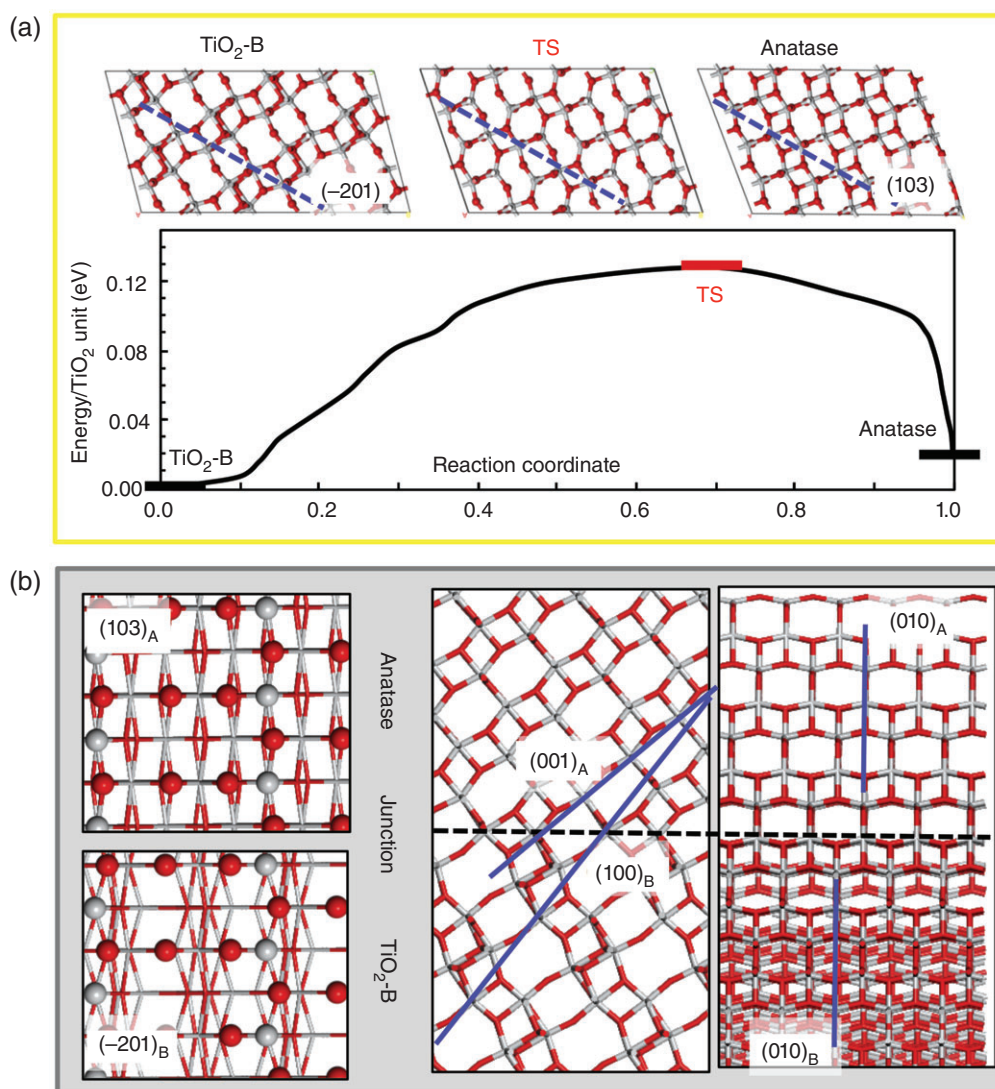
FIGURE 6 | (a) DFT lowest energy transition pathway from TiO$_2$(B) to anatase bulk crystal (structures viewed down from the *b* axis). The blue lines indicate the habit plane of the phase transition. (b) The atomic structure of the TiO$_2$(B)/anatase phase junction with orientationrelation $(\bar{2}\,0\,1)_B//(1\,0\,3)_A+[0\,1\,0]_B//[0\,1\,0]_A$ as predicted from theory. From left to the right are the top-views of (1 0 3)$_A$ and ((2) 0 1)$_B$, and two side-views of the junction showing the (1 0 0)$_B$ together with (0 0 1)$_A$ (theoretical dihedral angle 11.0 degrees), and (0 1 0)$_B$//(0 1 0)$_A$. Ti: gray; O: red. (Reprinted with permission from Ref 40. Copyright 2014 American Chemical Society)

matrix. The phase transition kinetics is found to be sensitive to the compressive strain and the crystallographic directions. The results rationalize the size and morphology dependence of the anisotropic phase transition kinetics of anatase particles.

CONCLUSION REMARKS

This article overviews the theoretical progress for characterizing the structure of 3*d* metal oxides and

understanding their photo-electrocatalytic activity in water splitting. For both the electronic and the geometrical structure complexity of these oxide catalysts, the OER on these catalysts has become one of the best testing-ground for advanced theoretical methods. In particular, recent years have seen increased applications of the automated PES exploration methods to search for new structures of these systems. For the bulk crystal structures, the latest global optimization methods has allowed the large-scale screening of crystal phases within the first principles framework
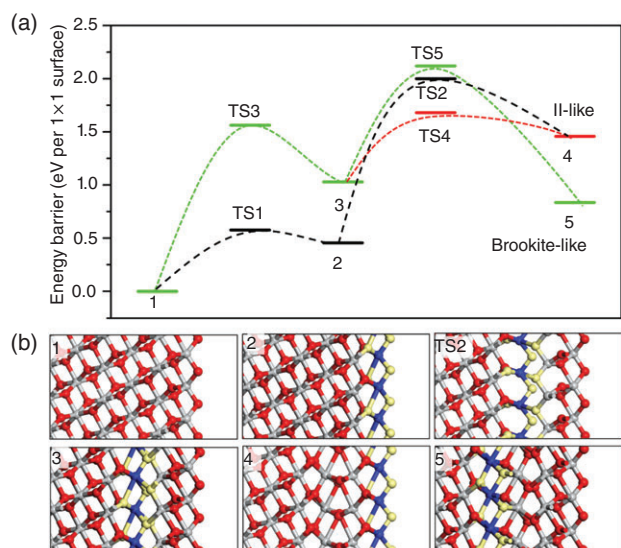
FIGURE 7 | (a) DFT energy profile and key structures for the anatase (1 1 2) reconstruction that leads to the formation of TiO_2-II and brookite phases. Blue: Ti after reconstruction; gray: Ti before reconstruction; yellow: O after reconstruction; and red: O before reconstruction. All views are looking down from anatase [1 1 0]. (Reprinted with permission from Ref 41. Copyright 2015 American Chemical Society)

since the primitive unit of crystals are generally small, e.g., within 40 atoms. The exploration of TiO_2 crystal PES has indeed led to the finding of several new crystal phases with desirable band gap for enhanced solar light adsorption, but the stability of these new phases at the ambient conditions is a general problem. The PES of Ni metal oxides also exhibits new energy-nearly-degenerate tunnel structures that have not been reported previously in experiment. The stability and the activity of these structures in OER remain to be explored.

Although the direct search of heterostructures composing multiple components using global optimization methods remains computationally impractical, the heterophase junction structure can now be solved indirectly based on the lowest energy crystal phase transition pathways. The SSW-based pathway sampling method provides a new approach to understand the kinetics stability of crystals and to reveal the

possible presence of coherent heterophase junctions. The stable heterophase junction requires the minimum strain at the interface and to achieve the best atom match between phases. The TiO_2-B/anatase heterophase junction has a simple low-strain interface. The crystallographic correspondence predicted from theory has an excellent agreement with the experimental observation. However, the SSW pathway sampling suggests a complex PES between anatase and rutile. Theory predicts a three-phase junction for anatase–rutile mixed phase oxides nucleating from anatase (1 1 2) surface and further demonstrates that the three-phase junction allows preferentially hole transfer from anatase to rutile.

The OER activity on TiO_2 surfaces has been investigated in a great detail with different theoretical methods, including advanced electronic structure methods (hybrid functional, post-DFT calculations), explicit solution molecular dynamics and periodic continuum solvation model. The first principles-based thermodynamics methods were proved to very successful for fast assessing the overall PES and predicting the key reaction step with the dominant energy cost in OER. The first proton removal step to produce adsorbed OH on TiO_2 surface is now known as the key rate-limiting step and the water splitting in this step follows the decoupled proton and electron transfer. The reaction step is both surface sensitive and phase sensitive, as the calculation shows that rutile (1 1 0) is much more active than anatase (1 0 1) for the heterolytic water splitting. These conclusions may also be transferable for understanding the water oxidation on the late transition metal oxides, where the similar reaction steps were found on Fe/Ni-based oxide surfaces. Because spin-polarized post-DFT calculations are generally required for late transition metal oxides, the high computational cost remains as a key challenge for the global structure search and the reaction pathway sampling. To date, the theoretical studies on the late transition metal oxides are limited and there are still many open questions on the active sites and the quantitative correlation between the OER activity and the catalyst structures.

REFERENCES

1. Fujishima A, Honda K. Electrochemical photolysis of water at a semiconductor electrode. *Nature* 1972, 238:37–38.

2. Lewis NS, Nocera DG. *Proc Natl Acad Sci USA* 2006, 103:15729–15735.

3. Kudo A, Miseki Y. Heterogeneous photocatalyst materials for water splitting. *Chem Soc Rev* 2009, 38:253–278.

4. Walter MG, Warren EL, McKone JR, Boettcher SW, Mi Q, Santori EA, Lewis NS. Solar water splitting cells. *Chem Rev* 2010, 110:6446–6473.

5. Grätzel M. Photoelectrochemical cells. *Nature* 2001, 414:338–344.

6. Linsebigler AL, Lu G, Yates JT Jr. Photocatalysis on TiO_2. *Chem Rev* 1995, 95:735–758.

7. Asahi R, Morikawa T, Ohwaki T, Aoki K, Taga Y. Visible-light photocatalysis in nitrogen-doped titanium oxides. *Science* 2001, 293:269–271.

8. Fujishima A, Zhang X, Tryk DA. TiO2 photocatalysis and related surface phenomena. *Surf Sci Rep* 2008, 63:515–582.

9. Diebold U. The surface science of titanium dioxide. *Surf Sci Rep* 2003, 48:53–229.

10. Henderson MA. A surface science perspective on TiO_2 photocatalysis. *Surf Sci Rep* 2011, 66:185–297.

11. Imanishi A, Okamura T, Ohashi N, Nakamura R, Nakato Y. Mechanism of water photooxidation reaction at atomically flat TiO_2 (Rutile) (110) and (100) surfaces: Dependence on solution pH. *J Am Chem Soc* 2007, 129:11569–11578.

12. Nakamura R, Imanishi A, Murakoshi K, Nakato Y. In situ FTIR studies of primary intermediates of photocatalytic reactions on nanocrystalline TiO_2 films in contact with aqueous solutions. *J Am Chem Soc* 2003, 125:7443–7450.

13. Takashima T, Hashimoto K, Nakamura R. Mechanisms of pH-dependent activity for water oxidation to molecular oxygen by MnO_2 electrocatalysts. *J Am Chem Soc* 2011, 134:1519–1527.

14. Chen J, Li Y-F, Sit P, Selloni A. Chemical dynamics of the first proton-coupled electron transfer of water oxidation on TiO_2 anatase. *J Am Chem Soc* 2013, 135:18774–18777.

15. Valdés A, Qu ZW, Kroes GJ, Rossmeisl J, Nørskov JK. Oxidation and photo-oxidation of water on TiO_2 surface. *J Phys Chem C* 2008, 112:9872–9879.

16. Li Y-F, Liu Z-P, Liu L, Gao W. Mechanism and activity of photocatalytic oxygen evolution on titania anatase in aqueous surroundings. *J Am Chem Soc* 2010, 132:13008–13015.

17. Gong M, Li Y, Wang H, Liang Y, Wu JZ, Zhou J, Wang J, Regier T, Wei F, Dai H. An advanced Ni—Fe layered double hydroxide electrocatalyst for water oxidation. *J Am Chem Soc* 2013, 135:8452–8455.

18. Smith RDL, Prévot MS, Fagan RD, Zhang Z, Sedach PA, Siu MKJ, Trudel S, Berlinguette CP. Photochemical route for accessing amorphous metal oxide materials for water oxidation catalysis. *Science* 2013, 340:60–63.

19. Trotochaud L, Ranney JK, Williams KN, Boettcher SW. Solution-cast metal oxide thin film electrocatalysts for oxygen evolution. *J Am Chem Soc* 2012, 134:17253–17261.

20. Landon J, Demeter E, İnoğlu N, Keturakis C, Wachs IE, Vasić R, Frenkel AI, Kitchin JR. Spectroscopic characterization of mixed Fe—Ni oxide electrocatalysts for the oxygen evolution reaction in alkaline electrolytes. *ACS Catal* 2012, 2:1793–1801.

21. Smith RDL, Prévot MS, Fagan RD, Trudel S, Berlinguette CP. Water oxidation catalysis: electrocatalytic response to metal stoichiometry in amorphous metal oxide films containing iron, cobalt, and nickel. *J Am Chem Soc* 2013, 135:11580–11586.

22. Li X, Walsh FC, Pletcher D. Nickel based electrocatalysts for oxygen evolution in high current density, alkaline water electrolysers. *Phys Chem Chem Phys* 2011, 13:1162–1167.

23. Louie MW, Bell AT. An investigation of thin-film Ni–Fe oxide catalysts for the electrochemical evolution of oxygen. *J Am Chem Soc* 2013, 135:12329–12337.

24. Ramírez A, Hillebrand P, Stellmach D, May MM, Bogdanoff P, Fiechter S. Evaluation of MnOx, Mn_2O_3, and Mn_3O_4 electrodeposited films for the oxygen evolution reaction of water. *J Phys Chem C* 2014, 118:14073–14081.

25. Fekete M, Hocking RK, Chang SLY, Italiano C, Patti AF, Arena F, Spiccia L. Highly active screen-printed electrocatalysts for water oxidation based on β-manganese oxide. *Energy Environ Sci* 2013, 6:2222–2232.

26. Najafpour MM, Haghighi B, Sedigh DJ, Ghobadi MZ. Conversions of Mn oxides to nanolayered Mn oxide in electrochemical water oxidation at near neutral pH, all to a better catalyst: catalyst evolution. *Dalton Trans* 2013, 42:16683–16686.

27. Gorlin Y, Lassalle-Kaiser B, Benck JD, Gul S, Webb SM, Yachandra VK, Yano J, Jaramillo TF. In situ x-ray absorption spectroscopy investigation of a bifunctional manganese oxide catalyst with high activity for electrochemical water oxidation and oxygen reduction. *J Am Chem Soc* 2013, 135:8525–8534.

28. Hamdani MRNS, Chartier P. Co_3O_4 and co-based spinel oxides bifunctional oxygen electrodes. *Int J Electrochem Sci* 2010, 5:556–577.

29. Gerken JB, McAlpin JG, Chen JYC, Rigsby ML, Casey WH, Britt RD, Stahl SS. Electrochemical water oxidation with cobalt-based electrocatalysts from pH 0–14: the thermodynamic basis for catalyst structure, stability, and activity. *J Am Chem Soc* 2011, 133:14431–14442.

30. Wales DJ, Doye JPK. Global optimization by basin-hopping and the lowest energy structures of Lennard-Jones clusters containing up to 110 atoms. *J Phys Chem A* 1997, 101:5111–5116.

31. Lyakhov AO, Oganov AR, Stokes HT, Zhu Q. New developments in evolutionary structure prediction algorithm USPEX. *Comput Phys Commun* 2013, 184:1172–1182.

32. Wu SQJM, Wang CZ, Nguyen MC, Zhao X, Umemoto K, Wentzcovitch RM, Ho KM. An adaptive genetic algorithm for crystal structure prediction. *J Phys Condens Matter* 2014, 26:035402.

33. Laio A, Parrinello M. Escaping free-energy minima. *Proc Natl Acad Sci USA* 2002, 99:12562–12566.

34. Martoňák R, Laio A, Parrinello M. Predicting crystal structures: the Parrinello-Rahman method revisited. *Phys Rev Lett* 2003, 90:075503.

35. Shang C, Liu ZP. Stochastic surface walking method for structure prediction and pathway searching. *J Chem Theory Comput* 2013, 9:1838–1845.

36. Zhang X-J, Shang C, Liu Z-P. From atoms to fullerene: stochastic surface walking solution for automated structure prediction of complex material. *J Chem Theory Comput* 2013, 9:3252–3260.

37. Shang C, Zhang XJ, Liu ZP. Stochastic surface walking method for crystal structure and phase transition pathway prediction. *Phys Chem Chem Phys* 2014, 16:17845–17856.

38. Glass CW, Oganov AR, Hansen N. USPEX—evolutionary crystal structure prediction. *Comput Phys Commun* 2006, 175:713–720.

39. Zhai H-J, Zhao Y-F, Li W-L, Chen Q, Bai H, Hu H-S, Piazza ZA, Tian W-J, Lu H-G, Wu Y-B, et al. Observation of an all-boron fullerene. *Nat Chem* 2014, 6:727–731.

40. Zhu S-C, Xie S-H, Liu Z-P. Design and observation of biphase TiO_2 crystal with perfect junction. *J Phys Chem Lett* 2014, 5:3162–3168.

41. Zhu S-C, Xie S-H, Liu Z-P. Nature of rutile nuclei in anatase-to-rutile phase transition. *J Am Chem Soc* 2015, 137:11532–11539.

42. Guan S-H, Zhang X-J, Liu Z-P. Energy landscape of zirconia phase transitions. *J Am Chem Soc* 2015, 137:8010–8013.

43. Zhu S-C, Guan S-H, Zhao W-N, Liu Z-P. Atomic structure of heterophase junction from theoretical prediction. *Top Catal* 2015, 58:644–654.

44. Shang C, Liu ZP. Constrained Broyden Dimer method with bias potential for exploring potential energy surface of multistep reaction process. *J Chem Theory Comput* 2012, 8:2215–2222.

45. Zhang X-J, Shang C, Liu Z-P. Double-ended surface walking method for pathway building and transition state location of complex reactions. *J Chem Theory Comput* 2013, 9:5745–5753.

46. Kilic MS, Bazant MZ, Ajdari A. Steric effects in the dynamics of electrolytes at large applied voltages. I. Double-layer charging. *Phys Rev E* 2007, 75:021502.

47. Borukhov I, Andelman D, Orland H. Steric effects in electrolytes: a modified Poisson-Boltzmann equation. *Phys Rev Lett* 1997, 79:435.

48. Andreussi O, Dabo I, Marzari N. Revised self-consistent continuum solvation in electronic-structure calculations. *J Chem Phys* 2012, 136:064102.

49. Hamada I, Sugino O, Bonnet N, Otani M. Improved modeling of electrified interfaces using the effective screening medium method. *Phys Rev B* 2013, 88:155427.

50. Gunceler D, Letchworth-Weaver K, Sundararaman R, Schwarz KA, Arias TA. The importance of nonlinear fluid response in joint density-functional theory studies of battery systems. *Model Simul Mater Sci Eng* 2013, 21:074005.

51. Fang Y-H, Liu Z-P. Mechanism and Tafel lines of electro-oxidation of water to oxygen on $RuO_2(110)$. *J Am Chem Soc* 2010, 132:18214–18222.

52. Koper MTM, van Santen RA. Electric field effects on CO and NO adsorption at the Pt(111) surface. *J Electroanal Chem* 1999, 476:64–70.

53. Patrito EM, Paredes-Olivera P. Surface science adsorption of hydrated hydroxide and hydronium ions on Ag(111). A quantum mechanical investigation. *Surf Sci* 2003, 527:149–162.

54. Hyman MP, Medlin JW. Theoretical study of the adsorption and dissociation of oxygen on Pt(111) in the presence of homogeneous electric fields. *J Phys Chem B* 2005, 109:6304–6310.

55. Panchenko A, Koper MTM, Shubina TE, Mitchell SJ, Roduner E. Ab initio calculations of intermediates of oxygen reduction on low-index platinum surfaces. *J Electrochem Soc* 2004, 151:A2016–A2027.

56. Karlberg GS, Rossmeisl J, Norskov JK. Estimations of electric field effects on the oxygen reduction reaction based on the density functional theory. *Phys Chem Chem Phys* 2007, 9:5158–5161.

57. Lozovoi AY, Alavi A. Reconstruction of charged surfaces: general trends and a case study of Pt(110) and Au(110). *Phys Rev B* 2003, 68:245416.

58. Lozovoi AY, Alavi A, Kohanoff J, Lynden-Bell RM. Ab initio simulation of charged slabs at constant chemical potential. *J Chem Phys* 2001, 115:1661–1669.

59. Sha Y, Yu TH, Merinov BV, Goddard WA III. DFT prediction of oxygen reduction reaction on

palladium-copper alloy surfaces. *ACS Catal* 2014, 4:1189–1197.

60. Sha Y, Yu TH, Merinov BV, Shirvanian P, Goddard WA III. Mechanism for oxygen reduction reaction on Pt₃Ni alloy fuel cell cathode. *J Phys Chem C* 2012, 116:21334–21342.

61. Sheng T, Lin WF, Hardacre C, Hu P. Significance of beta-dehydrogenation in ethanol electro-oxidation on platinum doped with Ru, Rh, Pd, Os and Ir. *Phys Chem Chem Phys* 2014, 16:13248–13254.

62. Groß A, Gossenberger F, Lin X, Naderian M, Sakong S, Roman T. Water structures at metal electrodes studied by ab initio molecular dynamics simulations. *J Electrochem Soc* 2014, 161:E3015–E3020.

63. Filhol JS, Doublet ML. An ab initio study of surface electrochemical disproportionation: the case of a water monolayer adsorbed on a Pd(111) surface. *Catal Today* 2013, 202:87–97.

64. Zhang T, Anderson AB. Parameter dependence in the local reaction center model for the electrochemical interface. *J Phys Chem C* 2009, 113:3197–3202.

65. Zhang T, Anderson AB. Oxygen reduction on platinum electrodes in base: theoretical study. *Electrochim Acta* 2007, 53:982–989.

66. Anderson AB, Neshev NM, Sidik RA, Shiller P. Mechanism for the electrooxidation of water to OH and O bonded to platinum: quantum chemical theory. *Electrochim Acta* 2002, 47:2999–3008.

67. Sidik RA, Anderson AB. Density functional theory study of O-2 electroreduction when bonded to a Pt dual site. *J Electroanal Chem* 2002, 528:69–76.

68. Anderson AB, Neshev NM. Mechanism for the electro-oxidation of carbon monoxide on platinum, including electrode potential dependence–theoretical determination. *J Electrochem Soc* 2002, 149: E383–E388.

69. Cai Y, Anderson AB. The reversible hydrogen electrode: potential-dependent activation energies over platinum from quantum theory. *J Phys Chem B* 2004, 108:9829–9833.

70. Fang Y-H, Liu Z-P. Tafel kinetics of electrocatalytic reactions: from experiment to first-principles. *ACS Catal* 2014, 4:4364–4376.

71. Cohen AJ, Mori-Sánchez P, Yang W. Insights into current limitations of density functional theory. *Science* 2008, 321:792–794.

72. Dudarev SL, Botton GA, Savrasov SY, Humphreys CJ, Sutton AP. Electron-energy-loss spectra and the structural stability of nickel oxide: an LSDA+U study. *Phys Rev B* 1998, 57:1505–1509.

73. Guo M, Zhang X-D, Du J. Electronic structure and enhanced visible-light absorption of N,B-codoped TiO₂. *Phys Status Solidi Rapid Res Lett* 2012, 6:172–174.

74. Mattioli G, Filippone F, Alippi P, Amore Bonapasta A. Ab initio study of the electronic states induced by oxygen vacancies in rutile and anatase. *Phys Rev B* 2008, 78:241201.

75. Jain A, Hautier G, Ong SP, Moore CJ, Fischer CC, Persson KA, Ceder G. Formation enthalpies by mixing GGA and GGA+U calculations. *Phys Rev B* 2011, 84:045115.

76. Mosey NJ, Liao P, Carter EA. Rotationally invariant ab initio evaluation of Coulomb and exchange parameters for DFT+U calculations. *J Chem Phys* 2008, 129:014103.

77. Li Y-F, Selloni A. Mechanism and activity of water oxidation on selected surfaces of pure and Fe-doped NiOx. *ACS Catal* 2014, 4:1148–1153.

78. Wang H-F, Kavanagh R, Guo Y-L, Guo Y, Lu G, Hu P. Origin of extraordinarily high catalytic activity of Co₃O₄ and its morphology chemistry for CO oxidation at low temperature. *J Catal* 2012, 296:110–119.

79. García-Mota M, Bajdich M, Viswanathan V, Vojvodic A, Bell AT, Nørskov JK. Importance of correlation in determining electrocatalytic oxygen evolution activity on cobalt oxides. *J Phys Chem C* 2012, 116:21077–21082.

80. Zasada F, Piskorz W, Stelmachowski P, Kotarba A, Paul J-F, Płociński T, Kurzydłowski KJ, Sojka Z. Periodic DFT and HR-STEM studies of surface structure and morphology of cobalt spinel nanocrystals. Retrieving 3D shapes from 2D images. *J Phys Chem C* 2011, 115:6423–6432.

81. Chen J, Selloni A. Electronic states and magnetic structure at the Co₃O₄(110) surface: a first-principles study. *Phys Rev B* 2012, 85:085306.

82. Li Y-F, Selloni A. Mosaic texture and double c-axis periodicity of β-NiOOH: insights from first-principles and genetic algorithm calculations. *J Phys Chem Lett* 2014, 5:3981–3985.

83. Himmetoglu B, Wentzcovitch RM, Cococcioni M. First-principles study of electronic and structural properties of CuO. *Phys Rev B* 2011, 84:115108.

84. Lee W-J, Kim Y-S. Linear-response calculation of the effective coulomb interaction between closed-shell localized electrons: Cu, Zn, and ZnO. *J Korean Phys Soc* 2012, 60:781–786.

85. Cowan AJ, Tang J, Leng W, Durrant JR, Klug DR. Water splitting by nanocrystalline TiO₂ in a complete photoelectrochemical cell exhibits efficiencies limited by charge recombination. *J Phys Chem C* 2010, 114:4208–4214.

86. Selcuk S, Selloni A. DFT+U study of the surface structure and stability of Co₃O₄(110): dependence on U. *J Phys Chem C* 2015, 119:9973–9979.

87. Cheng J, VandeVondele J, Sprik M. Identifying trapped electronic holes at the aqueous TiO_2 interface. *J Phys Chem C* 2014, 118:5437–5444.

88. Deskins NA, Dupuis M. Intrinsic hole migration rates in TiO_2 from density functional theory. *J Phys Chem C* 2008, 113:346–358.

89. Zhao WN, Zhu SC, Li YF, Liu ZP. Three-phase junction for modulating electron-hole migration in anatase/rutile photocatalysts. *Chem Sci* 2015, 6:3483–3494.

90. Ji YF, Wang B, Luo Y. Location of trapped hole on Rutile-TiO2(110) surface and its role in water oxidation. *J Phys Chem C* 2012, 116:7863–7866.

91. Nørskov JK, Rossmeisl J, Logadottir A, Lindqvist L, Kitchin JR, Bligaard T, Jónsson H. Origin of the overpotential for oxygen reduction at a fuel-cell cathode. *J Phys Chem B* 2004, 108:17886–17892.

92. Man IC, Su H-Y, Calle-Vallejo F, Hansen HA, Martínez JI, Inoglu NG, Kitchin J, Jaramillo TF, Nørskov JK, Rossmeisl J. Universality in oxygen evolution electrocatalysis on oxide surfaces. *ChemCatChem* 2011, 3:1159–1165.

93. Rossmeisl J, Qu ZW, Zhu H, Kroes GJ, Nørskov JK. Electrolysis of water on oxide surfaces. *J Electroanal Chem* 2007, 607:83–89.

94. Setvín M, Aschauer U, Scheiber P, Li Y-F, Hou W, Schmid M, Selloni A, Diebold U. Reaction of O_2 with subsurface oxygen vacancies on TiO_2 anatase (101). *Science* 2013, 341:988–991.

95. Li Y-F, Liu Z-P. Particle size, shape and activity for photocatalysis on titania anatase nanoparticles in aqueous surroundings. *J Am Chem Soc* 2011, 133:15743–15752.

96. Lee JH, Selloni A. TiO_2/ferroelectric heterostructures as dynamic polarization-promoted catalysts for photochemical and electrochemical oxidation of water. *Phys Rev Lett* 2014, 112:196102.

97. Cheng J, Sprik M. Acidity of the aqueous rutile TiO2(110) surface from density functional theory based molecular dynamics. *J Chem Theory Comput* 2010, 6:880–889.

98. Yoshihara T, Katoh R, Furube A, Tamaki Y, Murai M, Hara K, Murata S, Arakawa H, Tachiya M. Identification of reactive species in photoexcited nanocrystalline TiO_2 films by wide-wavelength-range (400-2500 nm) transient absorption spectroscopy. *J Phys Chem B* 2004, 108:3817–3823.

99. Tang J, Durrant JR, Klug DR. Mechanism of photocatalytic water splitting in TiO_2. Reaction of water with photoholes, importance of charge carrier dynamics, and evidence for four-hole chemistry. *J Am Chem Soc* 2008, 130:13885–13891.

100. Bahnemann DW, Hilgendorff M, Memming R. Charge carrier dynamics at TiO_2 particles: Reactivity of free and trapped holes. *J Phys Chem B* 1997, 101:4265–4275.

101. Yang X, Tamai N. How fast is interfacial hole transfer? In situ monitoring of carrier dynamics in anatase TiO_2 nanoparticles by femtosecond laser spectroscopy. *Phys Chem Chem Phys* 2001, 3:3393–3398.

102. Zhao W-N, Liu Z-P. Mechanism and active site of photocatalytic water splitting on titania in aqueous surroundings. *Chem Sci* 2014, 5:2256–2264.

103. Liao P, Keith JA, Carter EA. Water oxidation on pure and doped hematite (0001) surfaces: prediction of Co and Ni as effective dopants for electrocatalysis. *J Am Chem Soc* 2012, 134:13296–13309.

104. Bajdich M, García-Mota M, Vojvodic A, Nørskov JK, Bell AT. Theoretical investigation of the activity of cobalt oxides for the electrochemical oxidation of water. *J Am Chem Soc* 2013, 135:13521–13530.

105. Kanan MW, Nocera DG. In situ formation of an oxygen-evolving catalyst in neutral water containing phosphate and Co2+. *Science* 2008, 321:1072–1075.

106. Su HY, Gorlin Y, Man IC, Calle-Vallejo F, Nørskov JK, Jaramillo TF, Rossmeisl J. Identifying active surface phases for metal oxide electrocatalysts: a study of manganese oxide bi-functional catalysts for oxygen reduction and water oxidation catalysis. *Phys Chem Chem Phys* 2012, 14:14010.

107. Shang C, Zhao WN, Liu ZP. Searching for new TiO_2 crystal phases with better photoactivity. *J Phys Condens Matter* 2015, 27:134203.

108. Yang DJ, Liu HW, Zheng ZF, Yuan Y, Zhao JC, Waclawik ER, Ke XB, Zhu HY. An efficient photocatalyst structure: TiO2(B) nanofibers with a shell of anatase nanocrystals. *J Am Chem Soc* 2009, 131:17885–17893.

109. Carbone L, Cozzoli PD. Colloidal heterostructured nanocrystals: synthesis and growth mechanisms. *Nano Today* 2010, 5:449–493.

110. Casavola M, Buonsanti R, Caputo G, Cozzoli PD. Colloidal strategies for preparing oxide-based hybrid nanocrystals. *Eur J Inorg Chem* 2008:837–854.

111. Buonsanti R, Grillo V, Carlino E, Giannini C, Gozzo F, Garcia-Hernandez M, Garcia MA, Cingolani R, Cozzoli PD. Architectural control of seeded-grown magnetic-semicondutor iron oxide-TiO_2 nanorod heterostructures: the role of seeds in topology selection. *J Am Chem Soc* 2010, 132:2437–2464.

112. Buonsanti R, Grillo V, Carlino E, Giannini C, Curri ML, Innocenti C, Sangregorio C, Achterhold K, Parak FG, Agostiano A, et al. Seeded growth of asymmetric binary nanocrystals made of a semiconductor TiO_2 rodlike section and a magnetic gamma-Fe_2O_3 spherical domain. *J Am Chem Soc* 2006, 128:16953–16970.

113. Lazzarini L, Salviati G, Fabbri F, Zha M, Calestani D, Zappettini A, Sekiguchi T, Dierre B. Unpredicted

nucleation of extended zinc blende phases in wurtzite ZnO nanotetrapod arms. *ACS Nano* 2009, 3:3158–3264.

114. Zhao D, Zhang X, Zeng Q, Dong H, Li J, Cai L, Wang C, Zhou W, Xie S. A facile method to fabricate ultrathin vertical ZnO nanowall arrays. *J Nanosci Nanotechnol* 2013, 13:1291–1294.

115. Yoshida R, Suzuki Y, Yoshikawa S. Syntheses of $TiO_2(B)$ nanowires and TiO_2 anatase nanowires by hydrothermal and post-heat treatments. *J Solid State Chem* 2005, 178:2179–2185.

116. Li W, Liu C, Zhou YX, Bai Y, Feng X, Yang ZH, Lu LH, Lu XH, Chan KY. Enhanced photocatalytic activity in anatase/$TiO_2(B)$ core-shell nanofiber. *J Phys Chem C* 2008, 112:20539–20545.

117. Bai Y, Li W, Liu C, Yang ZH, Feng X, Lu XH, Chan KY. Stability of Pt nanoparticles and enhanced photocatalytic performance in mesoporous Pt-(anatase/$TiO_2(B)$ nanoarchitecture. *J Mater Chem* 2009, 19:7055–7061.

118. Zhou WJ, Gai LG, Hu PG, Cui JJ, Liu XY, Wang DZ, Li GH, Jiang HD, Liu D, Liu H, et al. Phase transformation of TiO_2 nanobelts and $TiO_2(B)$/anatase interface heterostructure nanobelts with enhanced photocatalytic activity. *CrystEngComm* 2011, 13:6643–6649.

119. Liu B, Khare A, Aydil ES. Interfaces TiO_2-B/anatase core-shell heterojunction nanowires for photocatalysis. *ACS Appl Mater Interfaces* 2011, 3:4444–4450.

120. Zheng ZF, Liu HW, Ye JP, Zhao JC, Waclawik ER, Zhu HY. Structure and contribution to photocatalytic activity of the interfaces in nanofibers with mixed anatase and $TiO_2(B)$ phases. *J Mol Catal A: Chem* 2010, 316:75–82.

121. Huang CX, Zhu KR, Qi MY, Zhuang YL, Cheng C. Preparation and photocatalytic activity of bicrystal phase TiO_2 nanotubes containing TiO_2-B and anatase. *J Phys Chem Solids* 2012, 73:757–761.

122. Brohan L, Verbaere A, Tournoux M, Demazeau G. Transformation $TiO_2(B)$→anatase. *Mater Res Bull* 1982, 17:355–361.

123. Penn RL. Imperfect oriented attachment: dislocation generation in defect-free nanocrystals. *Science* 1998, 281:969–971.

124. Wang Y, Cheng ZW, Tan SJ, Shao X, Wang B, Hou JG. Characterization of Cr–N codoped anatase $TiO_2(001)$ thin films epitaxially grown on $SrTiO_3(001)$. *Sur Sci.* 2013, 616:93–99.

125. Xia YB, Zhu K, Kaspar TC, Du YG, Birmingham B, Park KT, Zhang ZR. Atomic structure of the anatase $TiO_2(001)$ surface. *J Phys Chem Lett* 2013, 4:2958–2963.

126. Lazzeri MS, Selloni A. Stress-driven reconstruction of an oxide surface: the anatase TiO_2 (001)–(1×4) surface. *Phys Rev Lett* 2001, 87:266105.